Geng, Z., Bonnelye, A., David, C., Dick, P., Wang, Y., Schubnel, A. (2021): Pressure Solution Compaction During Creep Deformation of Tournemire Shale: Implications for Temporal Sealing in Shales. - Journal of Geophysical Research: Solid Earth, 126, 3, e2020JB021370.

https://doi.org/10.1029/2020JB021370

JGR Solid Earth

RESEARCH ARTICLE
10.1029/2020JB021370

Pressure Solution Compaction During Creep Deformation of Tournemire Shale: Implications for Temporal Sealing in Shales

Zhi Geng[1,2], Audrey Bonnelye[3], Christian David[4], Pierre Dick[5], Yanfei Wang[1,6], and Alexandre Schubnel[2]

[1]Key Laboratory of Petroleum Resources Research, Institute of Geology and Geophysics, Chinese Academy of Sciences, Beijing, China, [2]Laboratoire de Géologie de l'ENS (UMR 8538)–PSL Research University, Paris, France, [3]Helmholtz Center Potsdam GFZ German Research Center for Geosciences, Section 4.2 Geomechanics and Scientific Drilling, Telegrafeberg, Potsdam, Germany, [4]Département Géosciences & Environnement, Université de Cergy Pontoise, Cergy-Pontoise, France, [5]Institut de Radioprotection et de Sûreté Nucléaire (IRSN), France, [6]University of Chinese Academy of Sciences, Beijing, China

Key Points:

- The creep failure strength of Tournemire shale is greater than the short-term peak strength by ~60% at low and high pressures
- Pressure solution sealing in dolomite-rich shale is the most active at middle-shallow depth (e.g., ~3.8 km) conditions
- Significant strength and sealing capacity change are possible in shale, and the magnitude of change may be larger than expected

Supporting Information:

- Supporting Information S1

Correspondence to:
Z. Geng and Y. Wang,
gengzhi@mail.iggcas.ac.cn;
yfwang@mail.iggcas.ac.cn

Citation:
Geng, Z., Bonnelye, A., David, C., Dick, P., Wang, Y., & Schubnel, A. (2021). Pressure solution compaction during creep deformation of Tournemire shale: Implications for temporal sealing in shales. *Journal of Geophysical Research: Solid Earth*, *126*, e2020JB021370. https://doi.org/10.1029/2020JB021370

Received 14 NOV 2020
Accepted 8 JAN 2021

Abstract The temporal evolution of gouge compaction determines fluid transfer and rock rupture dynamics. Thus, studies on the time-dependent creep compaction processes of shale materials may elucidate the chemo-mechanical behavior of shallow clay-rich zones. We investigated this problem by combining creep experiments conducted in triaxial compression under upper crustal conditions with modeled pressure solution processes in Tournemire shale. The shale samples were deformed parallel and perpendicular to the bedding at low (10 MPa, 26°C, this study) and high (80 MPa, 26°C, published by Geng et al., 2018, https://doi.org/10.1029/2018JB016169) pressures. We monitored the deformation during stepping creep experiments until sample failure. Our results differ from those of traditional creep experiments and show that the creep failure strength of Tournemire shale samples increased significantly (by ~64%) at both pressures. Our experiments suggest that at appropriate temperatures, the pressure solution is highly active and is the dominant temporal sealing mechanism in the shale. Using our experimental data and the statistical rock physics method, we modeled the temporal reduction of effective porosity in terms of depth and temperature. Our thermal-stress coupled modeling results suggest that the pressure solution induced sealing is the most active at middle-shallow depths (~3.8 km). We believe that the sealing capacity and creep failure strength of dolomite-rich shales may change significantly at middle-shallow depths, indicating an important influence on reservoir fluids transfer and fault gouge strength.

Plain Language Summary The slow deformation of shale during inter-seismic periods results in the temporal evolution of fault gouge strength and impacts fluids transfer. Clay-rich materials are ubiquitous in reservoirs and fault zones, but the stress and temperature coupled compaction processes has not been well-studied quantitatively under shallow depth conditions. Traditional laboratory knowledge shows that rocks fail easier at lower loading rates. However, we showed that the failure strength for Tournemire shale increased significantly during long-term deformation experiments performed at different pressures. We suggested that a chemo-mechanical "pressure solution" process in dolomite-rich shale was the most active at middle-shallow depth conditions (~3.8 km). Our study indicates that sealing capacity and natural strength gain of shale fault gouges may increase at middle-shallow depths for a relatively short period of time (<3 years), influencing fluids transfer and seismic/aseismic cycles.

1. Introduction

Field observations and experimental studies reveal that crack sealing and creep compaction process determine the strength gain/recovery of rocks during inter-seismic periods (Bos & Spiers, 2002; Dieterich, 1972; Heimpel, 1997; Marone, 1998). The strength of the rupture zone may drop after the main shock and vary over the seismic cycle (Y. G. Li & Vidale, 2001; Marone et al., 1995; Vidale, 1994). The temporal sealing rate and strengthening of fault zones affects the fluid transfer along faults (Gratier et al., 2003) and earthquake recurrence time before failure (Marone et al., 1995; Tenthorey et al., 2003). Depending on pressure, temperature, and loading stress conditions, a rock can fail by shear-localization or cataclastic flow (T. F. Wong

et al., 1997), or be deformed by plastic flow developed through dislocation and diffusive mass transfer (Paterson & Wong, 2005). The post-seismic deformation rates gradually decrease by sealing processes on a scale of years to decades (Y. G. Li & Vidale, 2001), or are accelerated by seismic fracturing (Gratier et al., 2014). Active deformation mechanisms underlying this mechanical behavior include grain rearrangement, micro-cracking, subcritical crack growth, dislocation gliding, and diffusive mass transfer promoted by pressure solution processes. Significant progress has been made in understanding brittle to semi-brittle failures (Fredrich et al., 1989; Nicolas et al., 2017a; Paterson & Wong, 2005; T. F. Wong et al., 1997), but most studies primarily focus on underlying mechanical processes instead of chemo-mechanical interactions (Arson & Vanorio, 2015; Vanorio et al., 2011). Evidence suggests that chemical fluid-rock interaction processes, such as crack sealing and creep compaction, might enhance the sealing capacity and inter-seismic strength gain/recovery of rocks (Beeler et al., 2001; Hickman & Evans, 1995; Lang et al., 2015).

Laboratory studies highlight the significant role of sealing and compaction processes in cracks and fault gouges during the earthquake cycle and suggest pressure solution as a controlling mechanism (Fisher & Knipe, 1998; Yasuhara et al., 2005). Pressure solution creep is a chemo-mechanical process that dominates naturally occurring time-dependent deformations and occurs at temperatures lower than those required for dislocation creeps (Kerrich, 1974). Pressure solution involves shape changes of grains and mass transfer by dissolution, diffusion, and precipitation of minerals activated by stress-induced differences of chemical potentials (Pluymakers & Spiers, 2015; Rutter & Elliott, 1976; Spiers et al., 1990). Renard et al (2000) and Pluymakers and Spiers (2015) modeled compaction creep based on pressure solution kinetics around active faults and highlighted the role of fracture sealing in the seismicity recurrence time in field conditions. The majority of experimental and modeling studies on pressure solution focus either on frictional strength (resistance to sliding deformation), or hydraulic sealing of contact zones, using simulated gouges (quartzo-feldspathic, halite and calcite materials, Beeler & Tullis, 1997; Bos & Spiers, 2002; Hickman & Evans, 1992; Yasuhara et al., 2005) and quartz-rich stones (Lang et al., 2015; Yasuhara et al., 2004). However, shale materials are also ubiquitous in hydrocarbon reservoirs and fault gouges such as hard, massive gray-black shale in the foliated fault gouge in the southwest deformation zone of the active San Andreas Fault (Carpenter et al., 2015) and carbon shale in the Wenchuan Earthquake Fault (H. Li et al., 2013). The plausible rates, controlling stress and temperature of pressure solution in clay-rich materials during compactive creep deformation have not been quantitatively well-studied under upper crustal conditions.

In this study, we investigated the coupled impacts of time, stress and temperature during compaction creep produced by chemo-mechanical pressure solution interactions in clay-rich materials deformed in the shallow to middle-depth (<~8,000 m) conditions. Bonnelye et al. (2017) deformed Tournemire shale samples using the constant strain rates method at confining pressures ranging from 2.5 to 160 MPa and showed that the samples failed in a semi-brittle manner at confining pressure of 80 MPa. We published the rate-dependent operative mechanisms (individually and together) for Tournemire shale during creep deformation at a confining pressure of 80 MPa (semi-brittle regime) at room (26°C) and high (75°C) temperatures (Geng et al., 2018). Here, we first enriched the experimental data for samples deformed at a low confining pressure (10 MPa, brittle regime) and room temperature (26°C). We then simulated the pressure solution process using a statistical method (Appendix A) taking into account the experimental uncertainties, for which the parameters were constrained in our creep experiments. By modeling the evolution of effective porosity, we provided a temporal-thermal-stress coupled explanation for high sealing capacity in shale during compaction creep deformation. Our results reveal that the shale compaction and strengthening with the underlying chemo-mechanical mechanisms during creep deformation is highly active at middle-shallow depth (~3.8 km) conditions.

2. Experimental Methods

We used cylindrical shale samples (diameters of 42 ± 1 mm, lengths of 84.5 ± 0.1 mm) cored in situ from the Toarcian layer at the Tournemire site (Aveyron, France). The samples were from the same batch used by Bonnelye et al. (2017) and Geng et al. (2017). The weight proportions of clay materials (illite, smectite, and kaolinite), quartz, and calcite and dolomite in Tournemire shale are 30%~50%, 10%~20%,

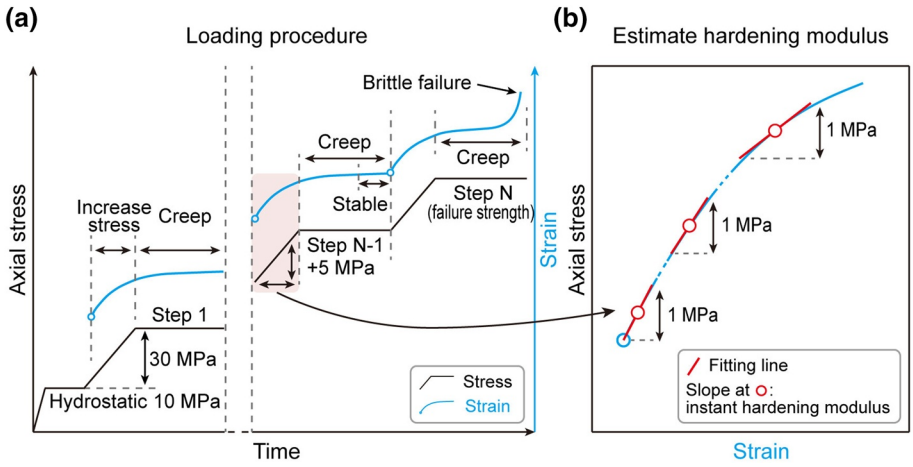

Figure 1. Experimental illustrations. (a) Loading procedure of creep experiments. (b) Method used to estimate the evolution of the instant hardening modulus of samples during increasing loading stress.

and 10%~30%, respectively (Bonin, 1998; Tremosa et al., 2012). Calcite and dolomite are prone to the pressure solution process. Natural pore water in the material varies from 3.5% to 8% (Bonin, 1998; Masri et al., 2014). A more detailed discussion on the physical properties of the material can be found in Boisson et al. (2001); Bonin, (1998); Schmitt et al. (1994); Tremosa et al. (2012). As Tournemire shale is transversely isotropic with respect to the bedding orientation, we used the samples with horizontal and vertical bedding to approximate the average mechanical and chemical responses of the clay-rich material during creep deformation.

Following the experimental protocol used in Geng et al. (2018), we performed the stepping creep experiments at a confining pressure of 10 MPa (Figure 1a). We first loaded the samples under hydrostatic conditions up to 10 MPa at a pressure rate of 0.3 MPa/min. Hydrostatic conditions were maintained for ~18 h at 26°C. Next, differential stress (axial stress minus confining pressure) was increased to a fixed initial stress (30 MPa) and maintained (creep status) for 24 h. The differential stress was repeatedly increased by 5 MPa and maintained for 24 h, until brittle failure. All the experiments were conducted using the triaxial apparatus installed at the Laboratoire de Géologie of ENS-Paris (France). There were few constraints on the natural saturation state of the samples because of their low permeability (10^{-19} to 10^{-21} m^2). To avoid exposition redundancy, an additional description of the technical performance of the triaxial apparatus can be referred to (Brantut et al., 2011; Sarout & Guéguen, 2008).

Compressive stresses and compactive strains are denoted as positive. Axial creep deformation was measured using three capacitive gap sensors that externally monitored the overall axial displacement of the piston during creep deformation. Volumetric strain during creep was estimated by adding the average of axial strains (axial displacement of the piston divided by the sample length) and two average radial strains measured by four radial strain gauges glued uniformly around the cylindrical rock surface. As the deformation rate generally stabilized during the last 8 h (Figure 1a) in most creep periods (Geng et al., 2018), we estimated the average axial strain rate over the last 8 h of each step to characterize the creep strain rate under the corresponding axial loading stress. More technical details of the sample configuration and creep rates estimation can be found in Geng et al. (2018).

In this study, the hardening modulus is defined as the derivative of the differential stress (σ) to the total axial strain (ε_t), that is, $H = d\sigma / d\varepsilon_t$. To characterize the hardening evolution of samples during increased differential stress (denoted by shaded area in Figure 1a), we estimated the instant hardening modulus, which were the slopes of the linear fittings of the stress-strain curves evaluated at stress intervals of 1 MPa (Figure 1b). The strength gain (%) is defined as $S_g = \left(\sigma_{cf} - \sigma_{st}\right) / \sigma_{st}$, where σ_{cf} is the differential stress at creep failure over a long deformation time-scale (~10 days), σ_{st} is the peak differential stress for samples deformed using a constant axial strain rate ($\sim 10^{-7}/s$) over a short time-scale (~24 h).

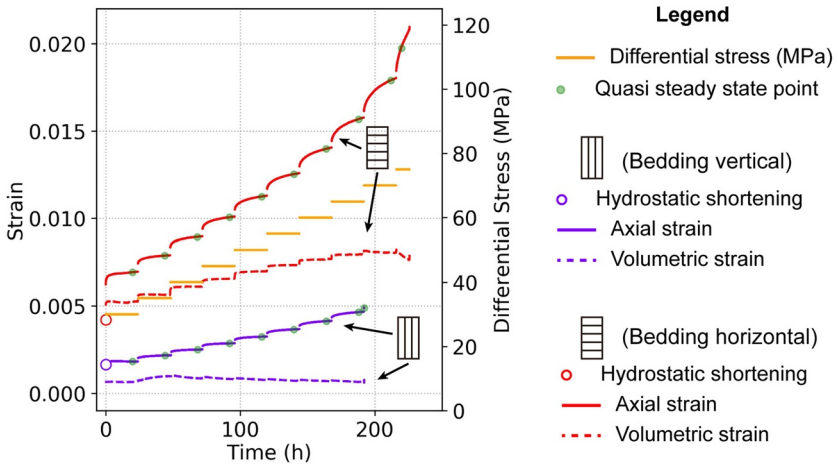

Figure 2. Creep deformation of samples with vertical and horizontal beddings under a confining pressure of 10 MPa.

3. Results and Discussion

3.1. Experimental Deformation

Figure 2 shows the creep deformation induced by stepwise axial loading at a confining pressure of 10 MPa. The axial shortening during hydrostatic loading is nearly two times larger for horizontal than for vertical bedding, indicating anisotropic initial compaction in the shale samples. The volumetric strain of the vertical bedding samples increased slightly during the first two stress steps and kept stable until creep failure. For the horizontal bedding sample, however, the volumetric strain continued increasing until instant brittle failure occurred. Thus, the creep compaction in the horizontal bedding sample is significantly larger than that in the vertical bedding sample. Additionally, the creep failure strain at low pressure (10 MPa) is 25%–50% that at high pressure (80 MPa; Geng et al., 2018) (Table 1).

We summarized the differential stress and strain data to compare the creep failure strength of Tournemire shale deformed under various conditions (Table 1). Geng et al. (2017) observed significant strength gain (approximately 64% on average) in Tournemire samples with horizontal bedding during creep deformation at high pressure (80 MPa) and different temperatures (26°C and 75°C). Bonnelye et al. (2017) reported strengths resulting from constant-strain-rate-loading. We observed remarkable average strength gains during creep of approximately 57% and 76% at 26°C at the low (10 MPa) and high (80 MPa) pressures, respectively. We attribute the variable strength gain of vertical bedding samples across the samples to anisotropy and shale variability. However, strength gain during the compaction

Table 1
Strength Gain of the Tournemire Shale Samples During Creep Deformation

Bedding	Pressure	*Long-term creep failurestrength and strain*	*Short-term failurestrength and strain*	Strength gain (%)
Vertical	Pc: 10 MPa Temp. 26°C	70 MPa (0.005)	48 MPa (0.004)	45.83
	Pc: 80 MPa Temp. 26°C	130 MPa (0.019)	71 MPa (0.009)	83.1
	Pc: 80 MPa Temp. 75°C	120 MPa (0.037)	–	69
Horizontal	Pc: 10 MPa Temp. 26°C	75 MPa (0.021)	44.6 MPa (0.014)	68.16
	Pc: 80 MPa Temp. 26°C	180 MPa (0.040)	106.5 MPa (0.032)	69.01
	Pc: 80 MPa Temp. 75°C	170 MPa (0.036)	–	59.62

Note: The short-term strength (peak differential stress for the samples deformed at a constant strain rate of $\sim 10^{-7}$ / s) was published by Bonnelye et al. (2017); the long-term creep failure strength for confining pressure of 80 MPa was published by Geng et al. (2018); the long-term creep failure strength for confining pressure of 10 MPa and calculated strength gain for various conditions were results in this study. The values in parentheses are the corresponding failure strains. The strength gain for samples deformed at 75°C was calculated using the corresponding values at 26°C for reference.

Table 2
Effective Petrophysical Parameters Used for Pressure-Solution Modeling During Tournemire Shale Creep Deformation

Parameter	Description	Effective value
Ω	Molar volume of dolomite ($m^3\ mol^{-1}$)	6.43×10^{-5} Chichagov (1994)
d	Effective grain size (m)	7×10^{-6}
Q_d	Apparent activation energy ($J\ mol^{-1}$)	2.6×10^4 Verberne (2015)
ϕ_0	Maxima effective porosity of the supporting grains	0.15
ϕ	Minima effective porosity of the grain aggregates	0.06

creep of the Tournemire shale samples exhibited only weak dependence on confining pressure. This was particularly noticeable for the horizontal bedding samples, which were analogous to vertical transverse isotropy media.

3.2. Mechanisms Revealed by Stress Sensitivity of Creep Strain Rates

We have illustrated the transition of the creep mechanism in Tournemire shale from the pressure solution to the stress corrosion micro-cracking during the stepwise loading of differential stress at a pressure of 80 MPa by fitting our simplified diffusional creep law based on (Gratier, 2011) as follows (Geng et al., 2018):

$$\dot{\varepsilon} = Ae^{3\Delta\sigma_n\Omega/RT}, s.t.\ \Delta\sigma_n \geq 30\ MPa \tag{1}$$

where $A = 8DSC_s\Omega / d^3$ (Table 2). Note that Equation 1 becomes linear in the semi-logarithmic plot $\left(\log_{10}\dot{\varepsilon} - \Delta\sigma_n\right)$, with a slope of 1.3 Ω/RT and intercept equal to $\log_{10}(A)$. We argued that the slope of approximately 0.015 (MPa^{-1}) indicated pressure-solution-induced creep deformation in Tournemire shale (Geng et al., 2018). In this work, the sensitivity of the strain rate k_{ps} at low pressure (10 MPa) is denoted as the slope of the fitted solid line across major creep periods (Figures 3a and 3b) and ranges from 0.015 to 0.02. The comparable results at low confining pressure indicate a potential pressure solution process during time-dependent deformation in the brittle regime. However, the creep rate of the first creep period deviated from the major trend of the pressure solution process, especially in the vertical bedding sample deformed at 10 MPa and 26°C (Figure 3a). Additionally, for the horizontal bedding sample deformed at low pressure, the creep strain rates extrapolated from low to high differential stress would be much higher than the strain rates of the samples deformed at high pressure (Figure 3b). A possible explanation is that for the horizontal bedding sample deformed at low pressure, the stress increment (30 MPa) of the first axial creep stress (40 MPa) is 6 times that of the following creep steps (5 MPa), and the corresponding loading time was only dozens of minutes, during which the sample was not equilibrated. Although the axial shortening of the two samples under hydrostatic loading was also quite different (Figure 2), and other processes may operate at low loading stress (Figures 3a and 3b), the k_{ps} values indicate comparable pressure solutions during major creep periods. When the samples approached final brittle failure, the deformation rates increased significantly. The corresponding k_d value from the data approaching sample failure (dashed lines) is higher by one order of magnitude, implying a distinct operative process.

Similar to the dilatant brittle creep failure of samples deformed at high pressure (80 MPa; Geng et al., 2018), the samples here (pressure of 10 MPa) also failed in a comparable way (Figure 3c). We showed that the stress exponent n (>10) of a power law relation (Equation 2 by Charles, 1958) widely used for brittle creep in rocks generally indicated a stress corrosion cracking process in Tournemire shale samples deformed at high pressure approaching failure (Geng et al., 2018):

$$\dot{\varepsilon} = Ce^{\frac{-Q_s}{RT}}\sigma^n \tag{2}$$

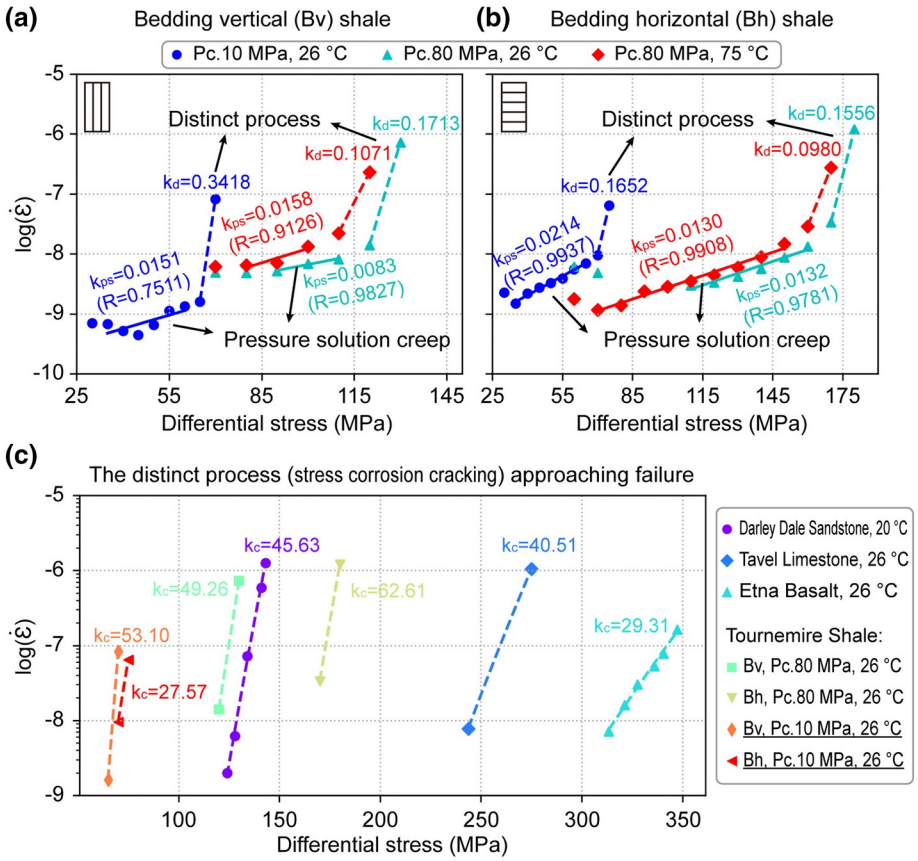

Figure 3. Stress sensitivity of creep in Tournemire shale samples with (a) vertical bedding and (b) horizontal bedding, deformed at a pressure of 10 MPa (this study) and 80 MPa (published by Geng et al., 2018). The axial strain rate data were fitted using a simplified creep law indicating a pressure solution mechanism by Geng et al. (2018). The data covered by the solid lines denote major creep periods, whereas the data crossed by the dashed lines were measurements approaching creep failure. The variable k_{ps} is the slope indicating the pressure solution creep; k_d is the slope implying a distinct process. (c) Comparison of the exponent n (k_c) in a power law relation (Equation 2 by Charles, 1958) revealing the stress corrosion cracking process during brittle creep. The data for comparison were from sandstone (Heap et al., 2009), limestone (Nicolas et al., 2017b), basalt (Heap et al., 2011), and the distinct process of the shale in Figures 3a and 3b. k_c is the slope of the fitted lines; the minimum correlation coefficient is 0.9973.

where C (MPa^{-n}/s) is a material constant, Q_s (J/mol) is the activation energy, R is the gas constant, T is the temperature (K), and σ (MPa) is the differential stress. Here, the slope k_c of Tournemire shale (n of Equation 2, see Figure 3c) ranges from 27 to 53, which is also comparable to the values of other rocks that underwent micro-cracking during steady state creep deformation. Thus, similar trends are observed at low (10 MPa, brittle regime) and high (80 MPa, semi-brittle regime) confining pressures. This describes the transition from compaction creep with the pressure solution as the dominant mechanism characterized by slope k_{ps} to brittle dilatant creep with micro-cracking characterized by slope k_c.

3.3. Mechanical Evidence for Strengthening

The hardening modulus evolution provided insight into the creep deformation mechanics as increasing the loading stress. Based on a kinematic balance equation, decomposing the total strain rate ($\dot{\varepsilon}_t$) into an elastic component ($\dot{\varepsilon}_{el}$) and a permanent component ($\dot{\varepsilon}_p$):

$$\dot{\varepsilon}_t = \dot{\varepsilon}_{el} + \dot{\varepsilon}_p = \frac{1}{K}\frac{d\sigma}{dt} + \dot{\varepsilon}_p \quad (3)$$

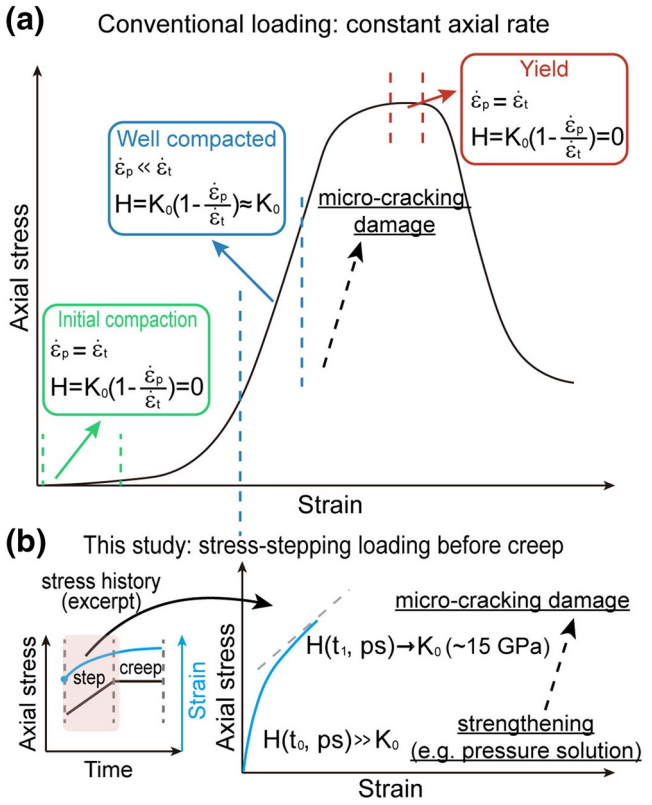

Figure 4. Illustration of hardening modulus evolution during loading and underlying mechanisms. (a) Conventional loading using a constant axial rate. (b) Stress-stepping loading for creep deformation. Shaded area (red) denotes stress-stepping period, that is, increasing differential stress using a constant axial rate (~10^{-7}/S) for the next creep period. Black arrows denote trends for underlying mechanisms.

where K is the appropriate elastic modulus, then gives:

$$\frac{d\sigma}{dt} = K\left(\dot{\varepsilon}_t - \dot{\varepsilon}_p\right) \tag{4}$$

According to our definition of the hardening modulus, then we have:

$$H \equiv \frac{d\sigma}{d\varepsilon_t} = \frac{d\sigma}{dt}\frac{dt}{\varepsilon_t} = \frac{d\sigma}{dt}\frac{1}{\dot{\varepsilon}_t} = K\left(1 - \frac{\dot{\varepsilon}_p}{\dot{\varepsilon}_t}\right) \tag{5}$$

Consider a scenario in conventional experiments loading the sample using a constant axial rate (Figure 4a), $\dot{\varepsilon}_p$ equals $\dot{\varepsilon}_t$ initially during the initial compaction period and $H = 0$. When the sample is deformed in a nearly elastic stage, $\dot{\varepsilon}_p / \dot{\varepsilon}_t \ll 1$ and the hardening modulus approximately equals K_0, which is stiffness (an elastic modulus) for the well compacted sample. However, the sample evolves gradually toward a yield stage along with micro-cracking damaging, and $\dot{\varepsilon}_p / \dot{\varepsilon}_t$ gently approaches 1, for which H is zero again. In other words, H is always no greater than K_0.

In this study, the results for hardening modulus evolution corresponded to the period of increasing differential stress up to the next constant stress for creep deformation (Figure 4b). The samples were well compacted at the end of both hydrostatic loading and each creep period. Thus, in the initial stage of increasing stress step before creep, $\dot{\varepsilon}_p / \dot{\varepsilon}_t \ll 1$ and $H_{\text{initial}} \approx K$. Note that the parameter K here is a function of time and potential pressure solution process for creep deformation. The values of H_{initial} were denoted by colorful circles in Figure 5. Those colorful circles indicated intrinsic stiffness resulting from temporal chemo-mechanical processes during the previous creep period. On the other hand, K_0 (~15 GPa) is effective average elastic moduli for our samples deformed by mechanical compaction only (see dash lines in Figure 5). Interestingly, although there was variability in samples, the average H_{initial} was significantly larger instead of smaller than both K_0 and the value for mechanical hydrostatic compaction (squares in Figure 5). Additionally, the subsequent values of H_{initial} (circles in Figure 5) remained stable with respect to creep periods. In summary, the mechanical responses suggested that the samples became stiffer at both confining pressures during creep compaction than during conventional deformation. It is a common sense that porous media becomes progressively stiffer when pore space is tightened by deformation (T. F. Wong & Baud, 2012). One should stress that such a significant temporal hardening cannot be explained solely by purely mechanical mechanisms.

3.4. Fully Coupled Thermal-Stress Modeling for Pressure Solution Creep

As indicated by our stress sensitivity results (Figures 3a and 3b), the pressure solution is active during the compaction creep under both confining pressures. Geng et al. (2018) showed, from the microscopic perspective, that time-dependent behavior was apparently controlled by creep compaction and shearing, implying a mixture of brittle and plastic deformation mechanisms. The veins with deposition constitute potential evidence of the diffusional pressure solution processes, which is the primary mechanism of crack sealing around active faults and in the gouge (Renard et al., 2000). For the shear-enhanced compaction band of Tournemire shale, Geng et al. (2017, 2018) showed pervasive indented grains, suggested as possible evidence of pressure solution processes during time-dependent deformation (Gratier et al., 1999). Although porosity reduction (or void filling) could be caused by other nearly-instantaneous processes such as grain

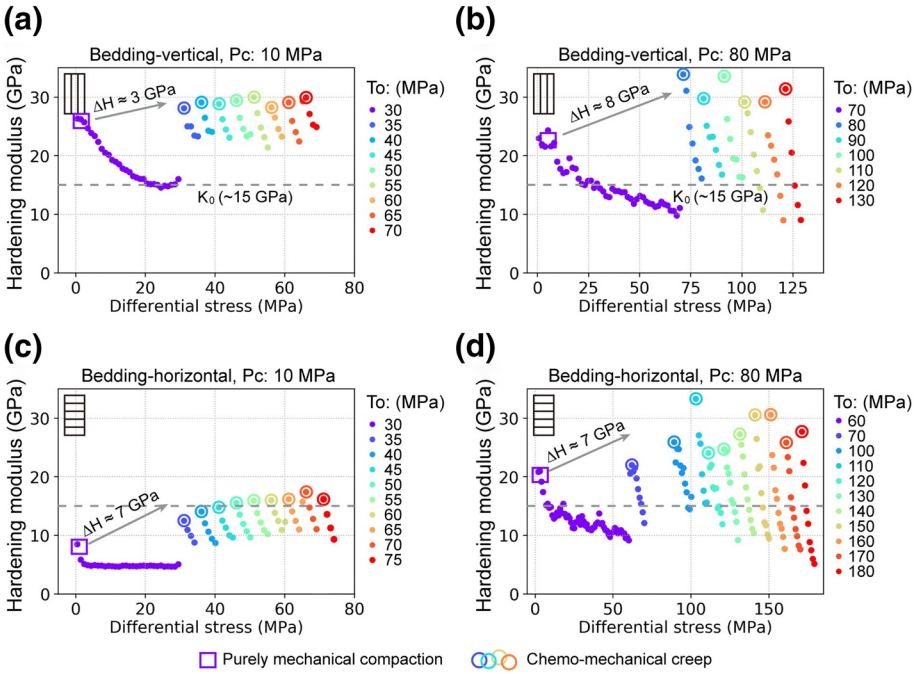

Figure 5. Evolution of hardening modulus during increasing differential stress up to the next constant stress for creep deformation in vertical bedding sample deformed at confining pressures of (a) 10 MPa and (b) 80 MPa, and in the horizontal bedding sample deformed at confining pressures of (c) 10 MPa and (d) 80 MPa, at room temperature (26°C). The color denotes the differential stress stage; the square indicates sample stiffness for purely mechanical compaction; the circle with a matching color indicates the start of the differential change and sample stiffness at each end of creep deformation. The horizontal dash lines denote K_0, which is effective average elastic moduli for our samples deformed by mechanical compaction only. The results in Figures 5b and 5d were calculated using data in Geng et al. (2018).

crushing and plastic pore collapse, the pressure solution dominates the longer-term/time-dependent compaction behavior and sealing time (Pluymakers & Spiers, 2015).

Unlike the use of grain geometry or strain for describing pressure solution creep (Gratier, 2011; Renard et al., 2000; Spiers et al., 1990), combining porosity to characterize aggregate structures (Pluymakers & Spiers, 2015) is a practical way to estimate creep compaction and sealing time. Pluymakers and Spiers (2015) proposed porosity-based models for compaction creep by dissolution-, diffusion-, and precipitation-controlled pressure solution. Here, we adopted their Model D3 (Pluymakers & Spiers, 2015) for the diffusion-controlled pressure solution that primarily describes the compaction strain rate in fault gouges under upper crustal conditions:

$$\dot{\varepsilon} = \frac{4\pi A_d Z}{F}\frac{DSC_s}{d^3}\frac{\sigma_n \Omega}{RT}\left(\frac{q}{q-2\phi}\right)^2 \tag{6}$$

in which $A_d = 2$ for pure 1D (uniaxial) compaction creep, and $A_d = 6$ for 3D isotropic compaction creep, $A_d = 3.7$ for this study constrained by experimental data; $Z = 6$ is the coordination number for a simple cubic pack of grains; F is the shape factor with a value of π; d is the mean grain diameter, m; DS is the product of the effective diffusion coefficient and the mean thickness of the grain boundary fluid film, $m^3 s^{-1}$; C_s is the average solubility of dissolved solid in the grain boundary fluid, $m^3 m^{-3}$; q is a geometric term equal to two times the maxima porosity (ϕ_0) of the pack of grains; ϕ is the current porosity of the grain aggregate; σ_n is the average normal stress, MPa; Ω is the molar volume of the solid phase, $m^3\ mol^{-1}$; R and T are the gas constant ($J\ mol^{-1}\ K^{-1}$) and absolute temperature (K), respectively.

Moreover, the value of DSC_s is sensitive to temperature through both the diffusion coefficient D and the solubility C_s. As suggested by Verberne (2015), we incorporated temperature sensitivity of DS depends on

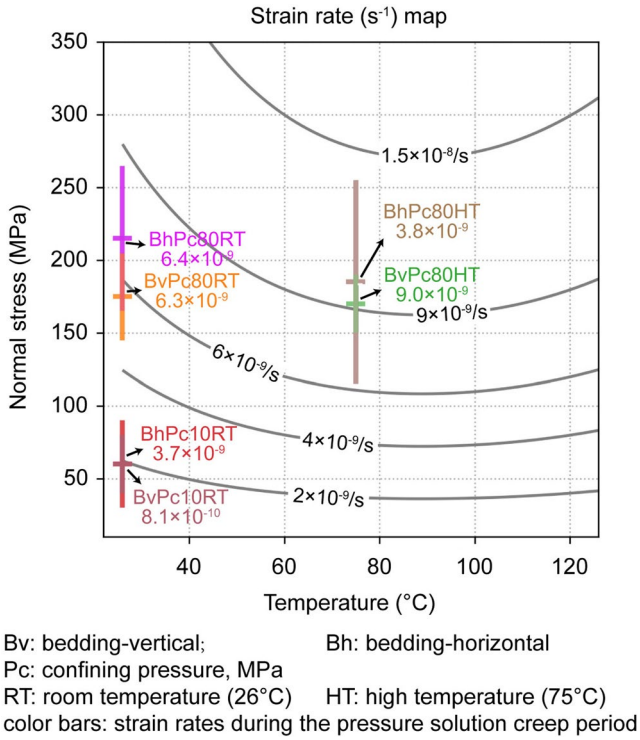

Figure 6. Pressure solution-induced strain rate map of Tournemire shale under upper-crustal conditions. The diffusion-controlled compaction strain rate was described by Model D3 in Pluymakers and Spiers (2015). The gray solid lines with strain rate labels are contour plots of the strain rate as a function of normal stress and temperature. The color bars denote our experimental conditions and average strain rates during the pressure solution creep period indicated in Figures 3a and 3b.

the value of the apparent activation energy (Q_d, $J\ mol^{-1}$) via an Arrhenius relation by:

$$DS = D_0 S e^{-Q_d/(RT)} \tag{7}$$

where $DS = 3\times10^{-18}\ m^3 s^{-1}$ *at* $T = 299K$, $Q_d = 2.3\times10^4$ *to* $2.9\times10^4\ J\ mol^{-1}$ constrained in this study. As dolomite solubility is also highly temperature sensitive for a wide temperature range, we coupled thermal impact to pressure solution creep of Tournemire shale by incorporating the solubility product constants for natural dolomite as a function of temperature (25°C–253°C) (Bénézeth et al., 2018) by:

$$log_{10} K_{sp^\circ-dol} = a + b/T + cT \tag{8}$$

where $K_{sp^\circ-dol}$ is solubility product constants, mol / L; T is absolute temperature, K; $a = 17.502$, $b = -4220.119$ and $c = -0.0689$. Then we approximated the C_s ($m^3 m^{-3}$) in Equation 6 based on mass action for dolomite reaction using:

$$\begin{aligned} C_s &= C_0 \Omega \\ &= 1000\left(K_{sp^\circ-dol}\right)^{0.25} \omega_{dol} \Omega \end{aligned} \tag{9}$$

where C_0 is solubility in the unstressed (hydrostatic) case, mol/m^3; $\omega_{dol} = 0.18$ is the effective weight proportion of dolomite in the sample. The values of the petrophysical parameters (Table 2) in the thermal-coupled model were constrained in our experimental measurements.

Our average experimental measurements for Tournemire shale creep generally agreed with the model results (Figure 6). The experimental results also show the strong anisotropy of creep in shales and the variability of measurements across the samples. Rock physics parameters, such as geometry and chemical properties, were also difficult to estimate from observations and provided the contribution to estimation uncertainty. However, overall, the diffusional creep model constrained by experiments partially shed light on time-dependent behavior beyond the laboratory scale. For the stress and temperature scale (Figure 6), the fully coupled thermal-stress analysis shows that strain rate was more sensitive to stress when the temperature was ~80°C–~90°C.

3.5. Pressure Solution Sealing and Induced Strength Gain

During time-dependent deformation, mechanical work is generally resolved in the chemical pressure solution process, which is the primary plastic rock deformation mechanism (Lehner, 1990; Spiers et al., 1990). Diffusive mass transfer during the pressure solution process contributes to micro-crack healing, fracture sealing, and porosity reduction (compaction sealing), which are widely observed in laboratory conditions (Bastiaens et al., 2007; Geng et al., 2017; Hilloulin et al., 2016; McNamara et al., 2016; Schubnel et al., 2005). Modeling of pressure-solution-induced crack sealing in quartz- and calcite-rich active faults shows that the sealing time ranges from years to millions of years (Bernabe & Evans, 2007; Gunzburger, 2010; Pluymakers & Spiers, 2015; Renard et al., 2000). However, fracture sealing in claystone and/or clay-rich samples has also been observed on laboratory time scales (Bastiaens et al., 2007; Bos & Spiers, 2001; Geng et al., 2017; Geng et al., 2018; Wang et al., 2013; C. L. Zhang, 2013).

Tenthorey et al. (2003) showed a strong correlation between fault strength and fault zone porosity after hydrothermal reactions and approximated the failure strength of samples using $P^* \propto (\phi R)^n$ (Zhang et al., 1990), where ϕ is the porosity, and R is the grain size. As explained by Tenthorey et al. (2003), the

equation $P^* \propto (\phi R)^n$ is based on Hertizan failure of contacting grains and should be valid to estimate the ultimate brittle failure strength of consolidated shear zones produced in the experiments. Because of the difficult justification of Hertizan fracturing in shale/clay-rich rocks, we used a similar empirical relation to correlate the temporal porosity and corresponding strength, as follows:

$$\sigma_p = A(\phi R)^n \tag{10}$$

where A and n are empirical constants. Then, we derived the strength gain as a function of porosity change only by:

$$\sigma_{gain} = \left(\frac{\phi}{\phi_0}\right)^n - 1 \tag{11}$$

where $n = -1.16$ was a first order approximation using average strength gain estimated from data for pressure solution creep periods in Figure 3, assuming the gained strength relative to the short-term peak strength was determined by effective porosity change.

Combining Equations 6 and 11, the time-dependent porosity, sealing time, and strength gain induced by pressure solution can be estimated by numerically integrating the expression ($\Delta t = \Delta\phi / \dot{\bar{\varepsilon}}$) for the porosity reduction from ϕ_0 to ϕ under upper-crustal conditions. Here, the porosity is an effective quantity of the supporting grain aggregate (mostly dolomite). We assumed that the normal stress is equal to the overburden stress with a gradient of 2.31 g/cm^3, the geothermal gradient is 30°C/km, the isotropic horizontal crustal stress is ~0.6 of the overburden stress, and the average volumetric strain rate ($\dot{\bar{\varepsilon}}$) is the sum of axial strain rate and two times the horizontal strain rate. At each depth point, we calibrated the value of ϕ_0 by removing the elastic bulk deformation for the corresponding pressure. The effective porosities were constrained by scanning electron microscopy (SEM) images of Tournemire shale samples (Figure S1). Table 2 summarizes the effective values of the above petrophysical parameters used for modeling based on our experimental constraints (Figure 6).

To present the modeling result with respect to the experimental uncertainties, we simulated the time-dependent change of the effective porosities of the sample and the corresponding strength gain (Figure 7) using a statistical method (see Appendix A) and diffusion-controlled pressure solution model (Equation 6), in which the parameters were constrained by our creep experiments (Figure 6). The predicted temporal porosities (solid curves in Figure 7) are statistical average results shown as time and depth profiles, indicating stress and temperature conditions.

By comparing the results between non-thermal coupled (Figures 7a, 7d, and 7g) and thermal coupled (Figures 7b, 7e, and 7h) modeling, we showed an important control of temperature to the pressure solution creep compaction in Tournemire shale. For non-thermal coupled modeling, we assumed the dolomite solubility and the diffusion coefficient in Equation 6 were constants and the creep strain rates were partially dependent on environmental temperature. The corresponding results for temporal porosity evolution up to 120 years (Figure 7) showed that porosity contour line space decreased with depth, indicating the pressure solution rate increased with increasing stress. However, for the fully thermal-coupled modeling, the results showed that significant temporal porosity change occurred at middle-shallow depth (~3.8 km) for relative short period of time (Figures 7b, 7e, and 7h). The overall uncertainty for average porosities decreased gradually over relative long period of time (Figures 7e and 7h). Interestingly, substantial evidence of both dissolution and reprecipitation at dolomite grain boundaries was observed in the sample deformed for only ~2 weeks at 75°C (Geng et al., 2018). It may be tempting to suggest that temperature has a critical impact on dolomite solubility and hence the creep rates within our experimental scales. In comparison, the modeling results of Gratier et al. (2003) for quartz-rich rocks showed that pressure solution rate kept increasing with depth (stress and geotemperature). However, for carbonate-rich rocks, the solubility of which is highly temperature sensitive, the pressure solution rate was the largest at depth around 3.5 km (Gratier et al., 2003). Similarly, our fully thermal-stress coupled modeling results for dolomite-rich shale implied that the pres-

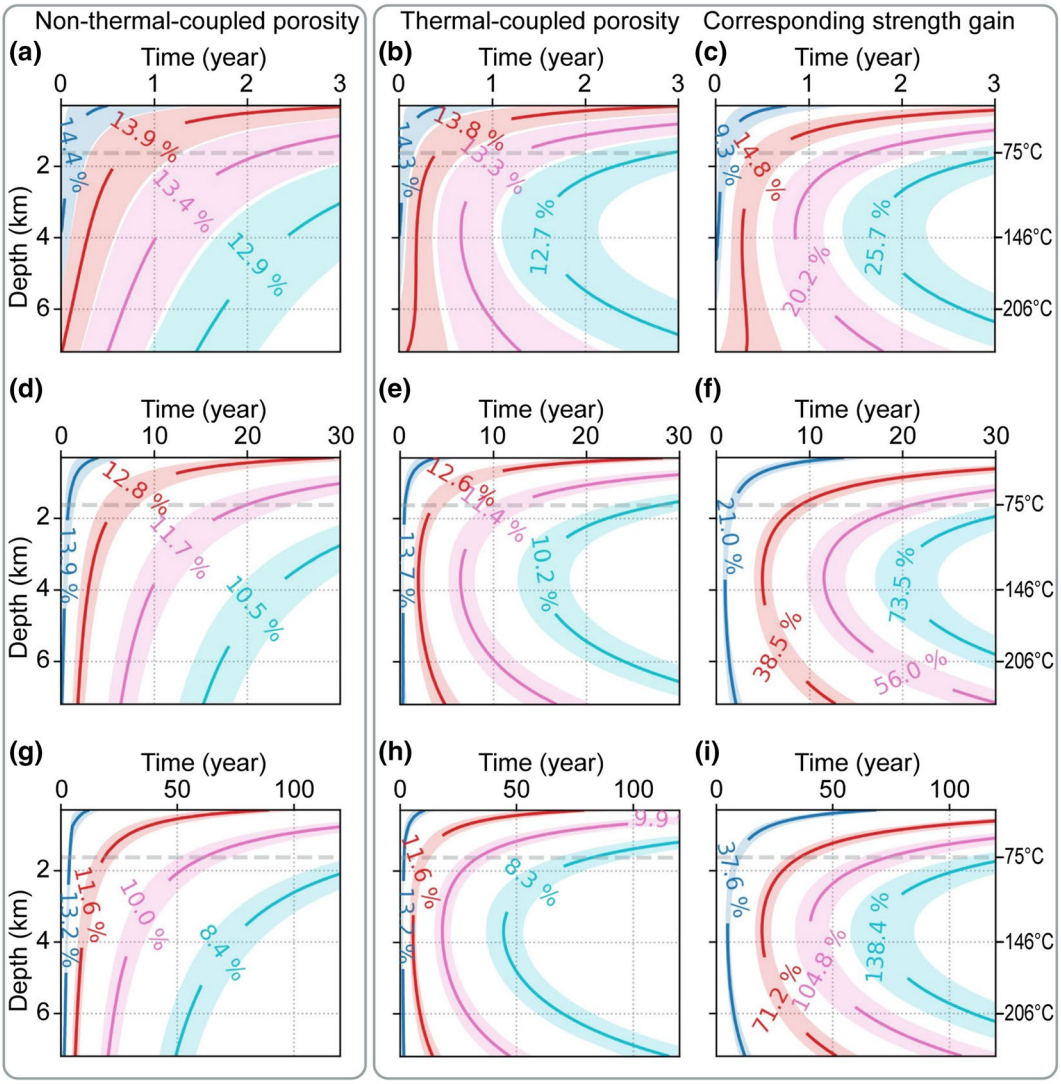

Figure 7. Statistical rock physics modeling of temporal porosity and strength gain by pressure-solution process in the geological environment. Simulation of no thermal-coupled temporal porosity evolution for 3 (a), 30 (d), and 120 (g) years. Simulation of fully thermal-coupled temporal porosity evolution for 3 (b), 30 (e), and 120 (h) years, and corresponding strength gain (c), (f), and (i), respectively. The areas with matching color denote ± 10% uncertainty with respective to the average value (solid lines).

sure solution compaction is the most active during creep deformation at middle-shallow depth (~3.8 km) and relatively low geotemperature (<~140°C) conditions.

The creep strain rate induced by the pressure solution of grains in Tournemire shale is likely overestimated, because other time-dependent deformation processes could also be active in shales. For example, crystal plasticity of supporting grains (Pluymakers & Spiers, 2015), enhanced kinetics of the pressure solution rate on clay mineral surfaces (Gundersen et al., 2002), and changes in the rheological properties by clay smearing (Gratier, 2011) may increase the rate of compaction. In this study, however, the temporal reduction in effective porosity and mass transfer was confirmed in Tournemire shale during pressure solution creep. This may be because mechanical compaction caused solely by external pressure was mostly accomplished during the 24-h hydrostatic loading before creep deformation, especially at high pressure (80 MPa). Additionally, with ongoing chemo-mechanical compaction, the temporal reduction of porosity contributes to

the recovery of elastic wave velocity (Schubnel et al., 2005; Vanorio & Mavko, 2011) (as suggested by Geng et al., 2018) and increases rock stiffness (T. F. Wong et al., 1997).

Compaction sealing are believed to result in significant strength gain under hydrothermal conditions (Bos & Spiers, 2002). Wiederhorn and Townsend (1970) reported high strength gain/recovery (approximately 80%) in cracks in soda-lime-silica glass specimens. A strength gain/recovery of 75% after 6 h of heating at 927°C was observed in sandstone samples from a fault gouge (Tenthorey et al., 2003). Rice (1978) suggested that the time-dependent healing of sharp micro-cracks may allow significant strength gain/recovery. The observed cementation processes (pressure solution of quartz and calcite infillings) in Alpine fault transition zone rocks featured reduced porosity and permeability, providing the potential for strength gain/recovery during the inter-seismic period (White & White, 1983). Micro-fractures may act as diffusion conduits for high-rate pressure solution processes that promote healing and sealing (Farver & Yund, 1998; J. P. Gratier & Gueydan, 2007). Cementation during pressure solution processes may also strongly contribute to the lithification and strengthening of the shale matrix (Angevine et al., 1982). Similarly, our Tournemire shale samples exhibited a strength gain of approximately 60% during creep and triaxial compaction at reservoir pressure (80 MPa) and relatively low geotemperatures (26°C and 75°C, Geng et al., 2017).

Strength gain/recovery during creep deformation in shales has not been given sufficient attention but can be inferred by the time-dependent evolution of porosity induced by pressure solution processes. We plotted the time-dependent strength gain of Tournemire shale corresponding to the thermal-stress coupled temporal porosities (Figures 7b, 7e, and 7h) using Equation 11 up to 120 years (Figures 7c, 7f, and 7i). We demonstrated that creep strain rates induced by pressure solution in Tournemire shale were sensitive to both stress and temperature within our experimental scales (Figure 6). The numerical analysis suggested that the temporal strength induced by pressure solution compaction would increase by ~70%, relative to the short-term failure strength, within 30 years for shale (Figure 7f). In comparison, the fault healing aided by pressure solution in quarzitic fault gouges requires nearly 104 years (Yasuhara et al., 2005). Renard et al. (2000) also argued that the time scale of pressure solution creep could be relatively small and gouge compaction is much faster than crack sealing. As it is very difficult to determine the exact loading stress at which the samples will fail under certain mechanism and within available laboratory time scales, the simulated strength gain by pressure solution is also likely overestimated. However, we report the differential stress at creep failure of Tournemire shale was significant greater relative to the short-term peak strength, which is counterintuitive in general. Additionally, we conclude that the temporal strength gain of dolomite-rich shale resulted from pressure solution cementation is most evident at middle-shallow depth (e.g. ~3.8 km) conditions.

4. Conclusion and Implication

We demonstrated that diffusional mass transfer is active during creep compaction in Tournemire shale in both brittle and semi-brittle deformation regimes. Pressure solution processes might have been the major mechanism operating during time-dependent deformation, especially at temperature of ~80°C. The significant strength gain (approximately 64%) at creep failure provided strong evidence to support shale compaction sealing. Modeling the pressure solution processes revealed that the creep strain rates in dolomite-rich shale are much more sensitive to stress when the temperature was ~80°C–~90°C. Pressure solution sealing would be more observable on the reservoir production time scale (e.g., 3–30 years) at middle-shallow depth (~3.8 km) than at deep depth conditions. Correspondingly, creep compaction is highly active at middle-shallow depth. The porosity loss and creep compaction could result in substantial strengthening. Accordingly, although the healing involving clay minerals could have a minor impact on strength gain/recovery (Tenthorey et al., 2003), our study suggests that significant strength gain is possible in dolomite-rich shale. With a knowledge of the mechanical-chemical compaction processes, it should be possible to predict the temporal strength gain. In such a situation, rupture intervals and associated stress drops in the shale fault gouge may be larger. However, the fast reduction of porosity from the pressure solution in the shallow formation also contributes to high sealing capacity, resulting in potential over-pressurization, fault weakening and earthquake nucleation. The upscaling analysis should be treated with caution, owing to the sensitivity and uncertainty of the petrophysical properties of shales and complex temporal variations during creep

deformation. More experiments are necessary to reduce risks associated with the thermal-stress analysis and provide robust pressure solution modeling for shale compaction and sealing.

Appendix A: Statistical Rock Physics Modeling for Pressure Solution Compaction

Based on the approach described in Section 3.4, we quantified the temporal porosity evolution induced by pressure solution using the Monte Carlo method with respect to our experimental estimation with uncertainty (Table A1). The Monte Carlo simulation is a powerful strategy to approximate derived distributions of average temporal porosity and corresponding strength gain by taking into account various distributions of petrophysical parameters. As a single "guess" input may give biased output, the statistical rock physics modeling is more robust than purely deterministic methods.

We assumed the parameters in Table A1 to be independently distributed with an average value of $A_d = 4.5$ valid for the crustal stresses setting, which are constants. As the weight content of crystal for pressure solution was estimated to be 0.18 here, we assumed the effective strain rate induced by pressure solution can be calibrated by a factor of 0.18. We drew 300 realizations from the parameter distributions defined in Table A1. Modeling depth ranged from 300–7,200 m at increments of 115 m. For each group of generated parameters, a time period was estimated for a small decrease step (0.0005) of porosity induced by pressure solution using Equation 6 and the expression ($\Delta t = \Delta\phi / \dot{\bar{\varepsilon}}$). By numerically integrating the process from ϕ_0 to ϕ, the pressure solution sealing time at specific depths was estimated; if the elapsed time meets the preseted time windows (e.g., 3, 30, or 300 years) or the current porosity reaches the lower limit value (0.06), the modeling is terminated; the corresponding strength gain at specific depths and times can be approximated using Equation 11. Finally, we presented the average porosity and temporal strength gain with ±10% uncertainty, from the derived distributions of the statistical modeling results (Figure 7). The modeling pseudocode was summarized in Table A2.

Table A1
Statistical Values Used for Temporal Porosity Reduction and Strength Gain Under Upper-Crustal Conditions for Tournemire Shale

Parameter	Description	Probability density function for the norm	Value boundary
d	Effective grain size (m)	U (5×10^{-6}, 9×10^{-6})	min: 5×10^{-6} max: 9×10^{-6}
A_d	2 for uniaxial compaction, 6 for 3D isotropic compaction	N (μ: 4.5, σ: 0.1)	min: 4.1
			max: 4.8
Q_d	Apparent activation energy ($J\ mol^{-1}$)	N (μ: 2.6×10^4, σ: 10^3)	min: 2.3×10^4
			max: 2.9×10^4
ϕ_0	Maxima effective porosity of the supporting grains	N (μ: 0.15, σ: 0.01)	min: 0.12
			max: 0.19
Φ	Minima effective porosity of the grain aggregates	N (μ: 0.06, σ: 0.01)	min: 0.03
			max: 0.09

Table A2
Pseudocode of Temporal Porosities Modeling

(1) Generate depth-time mesh grids;
(2) **For each** depth-time node:
(3) Draw random rock properties; calculate stress, temperature;estimate strain rate at ϕ_0 and at current porosity $\phi_t = \phi_0$−porosity decrement (*e.g.*, 0.0005);
(4) **While** elapsed time < node time *or* $\phi_t > \phi$*:*
(5) Estimate sealing time for the porosity decrement;
(6) Update ϕ_t, cumulate elapsed time;
(7) Process results (ϕ_t) statistically for grids

Data Availability Statement

The data produced during our experiments are archived in Zenodo (10.5281/zenodo.4422090).

Acknowledgments
This research was founded by IGGCAS Grant SZJJ201901, National Key R&D Program of China (2018YFC1504203; 2018YFC0603500) and by the European Research Council grant# ERC-2015-CoG: 681346–REALISM. The authors are grateful to Damien Deldicque for microscopy imaging support at ENS and to IRSN for technical support providing samples. The authors are grateful to Prof. Teng-Fong Wong, Dr. Martijn van den Ende, the Associate Editor, and the Editor for their constructive comments, which have greatly improved the manuscript.

References

Angevine, C., Turcotte, D., & Furnish, M. (1982). Pressure solution lithification as a mechanism for the stick-slip behavior of faults. *Tectonics*, *1*, 151–160. https://doi.org/10.1029/tc001i002p00151

Arson, C., & Vanorio, T. (2015). Chemomechanical evolution of pore space in carbonate microstructures upon dissolution: Linking pore geometry to bulk elasticity. *Journal of Geophysical Research: Solid Earth*, *120*, 6878–6894. https://doi.org/10.1002/2015jb012087

Bastiaens, W., Bernier, F., & Li, X. L. (2007). SELFRAC: Experiments and conclusions on fracturing, self-healing and self-sealing processes in clays. *Physics and Chemistry of the Earth, Parts A/B/C*, *32*, 600–615. https://doi.org/10.1016/j.pce.2006.04.026

Beeler, N., Hickman, S., & Wong, T. F. (2001). Earthquake stress drop and laboratory-inferred interseismic strength recovery. *Journal of Geophysical Research*, *106*, 30701–30713. https://doi.org/10.1029/2000jb900242

Beeler, N., & Tullis, T. (1997). The roles of time and displacement in velocity-dependent volumetric strain of fault zones. *Journal of Geophysical Research*, *102*, 22595–22609. https://doi.org/10.1029/97jb01828

Bénézeth, P., Berninger, U. N., Bovet, N., Schott, J., & Oelkers, E. H. (2018). Experimental determination of the solubility product of dolomite at 50–253 C. *Geochimica et Cosmochimica Acta*, *224*, 262–275. https://doi.org/10.1016/j.gca.2018.01.016

Bernabe, Y., & Evans, B. (2007). Numerical modelling of pressure solution deformation at axisymmetric asperities under normal load. *Geological Society London Special Publications*, *284*, 185–205. https://doi.org/10.1144/sp284.13

Boisson, J.-Y., Bertrand, L., Heitz, J.-F., & Golvan, Y. (2001). In situ and laboratory investigations of fluid flow through an argillaceous formation at different scales of space and time, Tournemire tunnel, southern France. *Hydrogeology Journal*, *9*, 108–123. https://doi.org/10.1007/s100400000119

Bonin, B. (1998). Deep geological disposal in argillaceous formations: Studies at the Tournemire test site. *Journal of Contaminant Hydrology*, *35*, 315–330. https://doi.org/10.1016/s0169-7722(98)00132-6

Bonnelye, A., Schubnel, A., David, C., Henry, P., Guglielmi, Y., Gout, C., et al. (2017). Strength anisotropy of shales deformed under uppermost-crustal conditions. *Journal of Geophysical Research: Solid Earth*, *122*, 110–129. https://doi.org/10.1002/2016jb013040

Bos, B., & Spiers, C. (2001). Experimental investigation into the microstructural and mechanical evolution of phyllosilicate-bearing fault rock under conditions favouring pressure solution. *Journal of Structural Geology*, *23*, 1187–1202. https://doi.org/10.1016/s0191-8141(00)00184-x

Bos, B., & Spiers, C. J. (2002). Fluid-assisted healing processes in gouge-bearing faults: Insights from experiments on a rock analogue system. *Pure and Applied Geophysics*, *159*, 2537–2566. https://doi.org/10.1007/s00024-002-8747-2

Brantut, N., Schubnel, A., & Guéguen, Y. (2012). Damage and rupture dynamics at the brittle-ductile transition: The case of gypsum. *Journal of Geophysical Research*, *116*, 20111978. https://doi.org/10.1029/2010JB007675

Carpenter, B., Saffer, D., & Marone, C. (2015). Frictional properties of the active San Andreas Fault at SAFOD: Implications for fault strength and slip behavior. *Journal of Geophysical Research: Solid Earth*, *120*, 5273–5289. https://doi.org/10.1002/2015jb011963

Charles, R. (1958). Static fatigue of glass. I. *Journal of Applied Physics*, *29*, 1549–1553. https://doi.org/10.1063/1.1722991

Chichagov, A. (1994). *Information-calculating system on crystal structure data of minerals (MINCRYST). Materials Science Forum*. 193–198. Trans Tech Publ.

Dieterich, J. H. (1972). Time-dependent friction in rocks. *Journal of Geophysical Research*, *77*, 3690–3697. https://doi.org/10.1029/jb077i020p03690

Farver, J. R., & Yund, R. A. (1998). Oxygen grain boundary diffusion in natural and hot-pressed calcite aggregates. *Earth and Planetary Science Letters*, *161*, 189–200. https://doi.org/10.1016/s0012-821x(98)00150-2

Fisher, Q. J., & Knipe, R. (1998). Fault sealing processes in siliciclastic sediments. *Geological Society, London, Special Publications*, *147*(1), 117–134. https://doi.org/10.1144/gsl.sp.1998.147.01.08

Fredrich, J. T., Evans, B., & Wong, T. F. (1989). Micromechanics of the brittle to plastic transition in Carrara marble. *Journal of Geophysical Research*, *94*, 4129–4145. https://doi.org/10.1029/jb094ib04p04129

Geng, Z., Bonnelye, A., Chen, M., Jin, Y., Dick, P., David, C., et al. (2017). Elastic anisotropy reversal during brittle creep in shale. *Geophysical Research Letters*, *44* 10887–810895. https://doi.org/10.1002/2017gl074555

Geng, Z., Bonnelye, A., Chen, M., Jin, Y., Dick, P., David, C., et al. (2018). Time and temperature dependent cin Tournemire shale. *Journal of Geophysical Research: Solid Earth*, *123*, 9658–9675. https://doi.org/10.1029/2018jb016169

Gratier (2011). Fault permeability and strength evolution related to fracturing and healing episodic processes (years to millennia): The role of pressure solution. *Oil & Gas Science and Technology–Revue d'IFP Energies nouvelles*, *66*, 491–506. https://doi.org/10.2516/ogst/2010014

Gratier, J.-P., Favreau, P., & Renard, F. (2003). Modeling fluid transfer along California faults when integrating pressure solution crack sealing and compaction processes. *Journal of Geophysical Research*, *108*(B2), 2104. https://doi.org/10.1029/2001jb000380

Gratier, J.-P., & Gueydan, F. (2007). Deformation in the presence of fluids and mineral reactions effect of fracturing and Fluid–Rock interaction on seismic cycles. In M. Handy, G. Hirth, J. Rice, N. Hovius, & A. Friedrich (Eds.,) *The Dynamics of Fault Zones*. MIT Press (pp. 319–356).

Gratier, J.-P., Renard, F., & Labaume, P. (1999). How pressure solution creep and fracturing processes interact in the upper crust to make it behave in both a brittle and viscous manner. *Journal of Structural Geology*, *21*, 1189–1197. https://doi.org/10.1016/s0191-8141(99)00035-8

Gratier, J.-P., Renard, F., & Vial, B. (2014). Postseismic pressure solution creep: Evidence and time-dependent change from dynamic indenting experiments. *Journal of Geophysical Research: Solid Earth*, *119*, 2764–2779. https://doi.org/10.1002/2013jb010768

Gundersen, E., Dysthe, D. K., Renard, F., Bjorlykke, K., & Jamtveit, B. (2002). Numerical modelling of pressure solution in sandstone, rate-limiting processes and the effect of clays. *Geological Society London Special Publications*, *200*, 41–60. https://doi.org/10.1144/gsl.sp.2001.200.01.03

Gunzburger, Y. (2010). Stress state interpretation in light of pressure-solution creep: Numerical modelling of limestone in the Eastern Paris Basin, France. *Tectonophysics*, *483*, 377–389. https://doi.org/10.1016/j.tecto.2009.11.005

Heap, M. J., Baud, P., Meredith, P., Bell, A., & Main, I. (2009). Time-dependent brittle creep in Darley Dale sandstone. *Journal of Geophysical Research*, *114*(B07203), https://doi.org/10.1029/2008jb006212

Heap, M. J., Baud, P., Meredith, P., Vinciguerra, S., Bell, A., & Main, I. (2011). Brittle creep in basalt and its application to time-dependent volcano deformation. *Earth and Planetary Science Letters*, *307*, 71–82. https://doi.org/10.1016/j.epsl.2011.04.035

Heimpel, M. (1997). Critical behaviour and the evolution of fault strength during earthquake cycles. *Nature*, *388*, 865. https://doi.org/10.1038/42232

Hickman, S. H., & Evans, B. (1992). Growth of grain contacts in halite by solution-transfer: Implications for diagenesis, lithification, and strength recovery. *International Geophysics: Elsevier*, *51*, 253–280. https://doi.org/10.1016/s0074-6142(08)62825-9

Hickman, S. H., & Evans, B. (1995). Kinetics of pressure solution at halite-silica interfaces and intergranular clay films. *Journal of Geophysical Research*, *100*, 13113–13132. https://doi.org/10.1029/95jb00911

Hilloulin, B., Legland, J.-B., Lys, E., Abraham, O., Loukili, A., Grondin, F., , &(2016). Monitoring of autogenous crack healing in cementitious materials by the nonlinear modulation of ultrasonic coda waves, 3D microscopy and X-ray microtomography. *Construction and Building Materials*, *123*, 143–152. https://doi.org/10.1016/j.conbuildmat.2016.06.138

Kerrich, R. (1974). *Aspects of pressure solution as a deformation mechanism*. University of London.

Lang, P. S., Paluszny, A., & Zimmerman, R. W. (2015). Hydraulic sealing due to pressure solution contact zone growth in siliciclastic rock fractures. *Journal of Geophysical Research: Solid Earth*, *120*(6), 4080–4101. https://doi.org/10.1002/2015jb011968

Lehner, F. K. (1990). *Thermodynamics of rock deformation by pressure solution*. Springer Netherlands.

Li, H., Wang, H., Xu, Z., Si, J., Pei, J., Li, T., et al. (2013). Characteristics of the fault-related rocks, fault zones and the principal slip zone in the Wenchuan Earthquake Fault Scientific Drilling Project Hole-1 (WFSD-1). *Tectonophysics*, *584*, 23–42. https://doi.org/10.1016/j.tecto.2012.08.021

Li, Y. G., & Vidale, J. E. (2001). Healing of the shallow fault zone from 1994–1998 after the 1992 M7. 5 Landers, California, earthquake. *Geophysical Research Letters*, *28*, 2999–3002. https://doi.org/10.1029/2001gl012922

Marone, C. (1998). Laboratory-derived friction laws and their application to seismic faulting. *Annual Review of Earth and Planetary Sciences*, *26*, 643–696. https://doi.org/10.1146/annurev.earth.26.1.643

Marone, C., Vidale, J. E., & Ellsworth, W. L. (1995). Fault healing inferred from time dependent variations in source properties of repeating earthquakes. *Geophysical Research Letters*, *22*, 3095–3098. https://doi.org/10.1029/95gl03076

Masri, M., Sibai, M., Shao, J.-F., & Mainguy, M. (2014). Experimental investigation of the effect of temperature on the mechanical behavior of Tournemire shale. *International Journal of Rock Mechanics and Mining Sciences*, *70*, 185–191. https://doi.org/10.1016/j.ijrmms.2014.05.007

McNamara, D. D., Lister, A., & Prior, D. J. (2016). Calcite sealing in a fractured geothermal reservoir: Insights from combined EBSD and chemistry mapping. *Journal of Volcanology and Geothermal Research*, *323*, 38–52. https://doi.org/10.1016/j.jvolgeores.2016.04.042

Nicolas, A., Fortin, J., & Guéguen, Y. (2017a). Micromechanical constitutive model for low-temperature constant strain rate deformation of limestones in the brittle and semi-brittle regime. *Geophysical Journal International*, *211*, 300–321. https://doi.org/10.1093/gji/ggx299

Nicolas, A., Fortin, J., Regnet, J., Verberne, B., Plümper, O., Dimanov, A., et al. (2017b). Brittle and semibrittle creep of Tavel limestone deformed at room temperature. *Journal of Geophysical Research: Solid Earth*, *122*, 4436–4459. https://doi.org/10.1002/2016jb013557

Paterson, M. S., & Wong, T.-f. (2005). *Experimental rock deformation-the brittle field*. Springer Science & Business Media.

Pluymakers, & Spiers, C (2015). Compaction creep of simulated anhydrite fault gouge by pressure solution: Theory V experiments and implications for fault sealing. *Geological Society, London, Special Publications*, *409*, 107–124. https://doi.org/10.1144/sp409.6

Renard, F., Gratier, J.-P., & Jamtveit, B. (2000). Kinetics of crack-sealing, intergranular pressure solution, and compaction around active faults. *Journal of Structural Geology*, *22*, 1395–1407. https://doi.org/10.1016/s0191-8141(00)00064-x

Rice, J. (1978). Thermodynamics of the quasi-static growth of Griffith cracks. *Journal of the Mechanics and Physics of Solids*, *26*, 61–78. https://doi.org/10.1016/0022-5096(78)90014-5

Rutter, E. H., & Elliott, D. (1976). The kinetics of rock deformation by pressure solution [and discussion]. *Philosophical Transactions of the Royal Society of London*, *283*, 203–219.

Sarout, J., & Guéguen, Y. (2008). Anisotropy of elastic wave velocities in deformed shales: Part 1—Experimental results. *Geophysics*, *73*, D75–D89. https://doi.org/10.1190/1.2952744

Schmitt, L., Forsans, T., & Santarelli, F. (1994). Shale testing and capillary phenomena. *International Journal Of Rock Mechanics And Mining Sciences & Geomechanics Abstracts*, *31*(5), 411–427 Elsevier.

Schubnel, A., Fortin, J., Burlini, L., & Gueguen, Y. (2005). Damage and recovery of calcite rocks deformed in the cataclastic regime. *Geological Society, London, Special Publications*, *245*, 203–221. https://doi.org/10.1144/gsl.sp.2005.245.01.10

Spiers, Schutjens, P. M. T. M., Brzesowsky, R. H., Peach, C. J., Liezenberg, J. L., & Zwart, H. J. (1990). Experimental determination of constitutive parameters governing creep of rocksalt by pressure solution. *Geological Society*, *54*, 215–227. https://doi.org/10.1144/gsl.sp.1990.054.01.21

Tenthorey, E., Cox, S. F., & Todd, H. F. (2003). Evolution of strength recovery and permeability during fluid–rock reaction in experimental fault zones. *Earth and Planetary Science Letters*, *206*, 161–172. https://doi.org/10.1016/s0012-821x(02)01082-8

Tremosa, J., Arcos, D., Matray, J., Bensenouci, F., Gaucher, E. C., Tournassat, C., & Hadi, J. (2012). Geochemical characterization and modelling of the Toarcian/Domerian porewater at the Tournemire underground research laboratory. *Applied Geochemistry*, *27*, 1417–1431. https://doi.org/10.1016/j.apgeochem.2012.01.005

Vanorio, T., & Mavko, G. (2011). Laboratory measurements of the acoustic and transport properties of carbonate rocks and their link with the amount of microcrystalline matrix. *Geophysics*, *76*(4), E105–E115. https://doi.org/10.1190/1.3580632

Vanorio, T., Nur, A., & Ebert, Y. (2011). Rock physics analysis and time-lapse rock imaging of geochemical effects due to the injection of CO 2 into reservoir rocks. *Geophysics*, *76*, O23–O33. https://doi.org/10.1190/geo2010-0390.1

Verberne, B. A. (2015). *Strength, stability, and microstructure of simulated calcite faults sheared under laboratory conditions spanning the brittle-plastic transition*. UU Department of Earth Sciences.

Vidale, J. (1994). Rupture variation with recurrence interval in eighteen cycles of a small earthquake. *Nature*, *368*, 624–626. https://doi.org/10.1038/368624a0

Wang, J.-J., Zhang, H.-P., Zhang, L., & Liang, Y. (2013). Experimental study on self-healing of crack in clay seepage barrier. *Engineering Geology*, *159*, 31–35. https://doi.org/10.1016/j.enggeo.2013.03.018

White, J., & White, S. (1983). Semi-brittle deformation within the Alpine fault zone, New Zealand. *Journal of Structural Geology*, *5*, 579–589. https://doi.org/10.1016/0191-8141(83)90070-6

Wiederhorn, S., & Townsend, P. (1970). Crack healing in glass. *Journal of the American Ceramic Society*, *53*, 486–489. https://doi.org/10.1111/j.1151-2916.1970.tb15996.x

Wong, T.-f., & Baud, P. (2012). The brittle-ductile transition in porous rock: A review. *Journal of Structural Geology*, *44*, 25–53. https://doi.org/10.1016/j.jsg.2012.07.010

Wong, T. f., David, C., & Zhu, W. (1997). The transition from brittle faulting to cataclastic flow in porous sandstones: Mechanical deformation. *Journal of Geophysical Research*, *102*, 3009–3025. https://doi.org/10.1029/96jb03281

Yasuhara, H., Elsworth, D., & Polak, A. (2004). Evolution of permeability in a natural fracture: Significant role of pressure solution. *Journal of Geophysical Research*, *109*(B3), B03204. https://doi.org/10.1029/2003jb002663

Yasuhara, H., Marone, C., & Elsworth, D. (2005). Fault zone restrengthening and frictional healing: The role of pressure solution. *Journal of Geophysical Research*, *110*. B06310. https://doi.org/10.1029/2004jb003327

Zhang, C.-L. (2013). Sealing of fractures in claystone. *Journal of Rock Mechanics and Geotechnical Engineering*, *5*, 214–220. https://doi.org/10.1016/j.jrmge.2013.04.001

Zhang, J., Wong, T. F., & Davis, D. M. (1990). Micromechanics of pressure-induced grain crushing in porous rocks. *Journal of Geophysical Research*, *95*, 341–352. https://doi.org/10.1029/jb095ib01p00341